Illuminating a Contorted Slab with a Complex Intraslab Rupture Evolution during the 2021 M_W 7.3 East Cape, New Zealand Earthquake

Ryo Okuwaki[1,2,3,=], Stephen P. Hicks[4,=], Timothy J. Craig[3], Wenyuan Fan[5], Saskia Goes[4], Tim J. Wright[3], and Yuji Yagi[2]

[1]Mountain Science Center, University of Tsukuba, Tsukuba, Ibaraki 305-8572, Japan

[2]Faculty of Life and Environmental Sciences, University of Tsukuba, Tsukuba, Ibaraki 305-8572, Japan

[3]COMET, School of Earth and Environment, University of Leeds, Leeds LS2 9JT, UK

[4]Department of Earth Science and Engineering, Imperial College London, London SW7 2AZ, UK

[5]Scripps Institution of Oceanography, UC San Diego, La Jolla, California 92093, USA

Key Points:

- A moment magnitude 7.3 2021 East Cape, New Zealand intraslab earthquake comprised multiple rupture episodes with different faulting styles
- The complex rupture comprises components of shallow trench-normal extension and unexpectedly, deep trench-parallel compression in slab
- The trench-parallel compression likely reflects stress rotation at a buoyancy contrast that drives slab contortion

[=]Equally contributing author

Corresponding author: Ryo Okuwaki, rokuwaki@geol.tsukuba.ac.jp

Abstract

The state-of-stress within subducting oceanic plates controls rupture processes of deep intraslab earthquakes. However, little is known about how the large-scale plate geometry and the stress regime relate to the physical nature of the deep-intraslab earthquakes. Here we find, by using globally and locally observed seismic records, that the moment magnitude 7.3 2021 East Cape, New Zealand earthquake was driven by a combination of shallow trench-normal extension and unexpectedly, deep trench-parallel compression. We find multiple rupture episodes comprising a mixture of reverse, strike-slip, and normal faulting. Reverse faulting due to the trench-parallel compression is unexpected given the apparent subduction direction, so we require a differential-buoyancy driven stress rotation which contorts the slab near the edge of the Hikurangi plateau. Our finding highlights that buoyant features in subducting plates may cause diverse rupture behavior of intraslab earthquakes due to the resulting heterogeneous stress state within slabs.

Plain Language Summary

A key type of tectonic boundary is where two plates collide with one sinking into the mantle beneath. These subduction zones generate the world's largest earthquakes. Quantifying stress in the subducting plate ("slab") is important because slabs drive the global plate-tectonic system, and large earthquakes can occur within them. These earthquakes can cause strong shaking, and, when occurring near cities, can lead to damage. However, mapping stress is challenging as we cannot directly "see" inside deep slabs. Our best indications of slab stress come from earthquakes themselves. A magnitude 7.3 earthquake north of New Zealand in 2021 generated a distinct pattern of seismic waveforms at seismometers installed worldwide. We used these seismic records to probe the earthquake, providing a new view of stress in subduction zones. We found the earthquake generated both vertical and horizontal motions along faults, driven by compressional and extensional stresses deep within the slab. The compressional part is oriented 90 degrees from the subduction direction, which is opposite to the usual compression in subduction zones, and has not been observed before. This unusual direction of compression can be explained by subduction of a thickened and buoyant part of the Pacific plate, known as the Hikurangi plateau.

1 Introduction

Complex fault configurations and heterogeneous fault conditions, i.e., stress and strength states, govern earthquake rupture development and propagation (Avouac et al., 2014; Floyd et al., 2016; Elliott et al., 2016; Hamling et al., 2017). Such relations can be inferred from the fault geometry and long-term geodetic observations for shallow active faults (Simons et al., 2002; Williams et al., 2013; Elliott et al., 2016; Arai et al., 2016; Hamling et al., 2017; Hayes et al., 2018; Sippl et al., 2018). However, for intraslab earthquakes occurring below ~50 km depth, these physical controlling factors are difficult to assess because of challenges to map structure at such depths, and the general lack of seismicity there (Wiens, 2001; Ranero et al., 2005; Page et al., 2016; Dascher-Cousineau et al., 2020; Gomberg & Bodin, 2021). In particular, the internal stress state and its extensional-compression transition regime are often elusive in subducted slabs, although they directly impact intraslab earthquake occurrence and their faulting styles (Astiz et al., 1988; Ammon et al., 2008; Craig et al., 2014; Romeo & Álvarez-Gómez, 2018; Sandiford et al., 2019, 2020; Ye et al., 2021). Thus, imaging the rupture processes of large, deep intraslab earthquakes offers a rare window to investigate the slab configuration, and to understand fault interaction and rupture evolution of these earthquakes, illuminating heterogeneous stress fields.

An intraslab moment magnitude (M_W) 7.3 earthquake occurred offshore the East Cape in northern New Zealand on 4th March 2021, which was followed ~4 hours later by a series of the M_W 7.4 and M_W 8.1 earthquakes in the Kermadecs (~900 km to the north) (GeoNet, 2021). The M_W 7.3 2021 East Cape earthquake, which is the focus of this paper, may offer insight into the regional slab geometry because of its location and complex rupture process. The 2021 East Cape earthquake locates at the boundary between the southern end of Kermadec trench and the northern end of Hikurangi margin, where the Pacific plate subducts beneath the Australian plate and its convergence decreases and progressively rotates to oblique motion toward the south (Fig. 1) (Collot et al., 1996, 2001; Lewis et al., 1998; Wallace et al., 2009). The reported centroid depth of the earthquake was ~50 km (U.S. Geological Survey Earthquake Hazards Program, 2017; Duputel et al., 2012; Dziewonski et al., 1981; Ekström et al., 2012), and the focal mechanism indicates oblique-thrust motion, with the compressional axis oriented towards the north-south direction (Fig. 1) (U.S. Geological Survey Earthquake Hazards Program, 2017; Duputel et al., 2012; Dziewonski et al., 1981; Ekström et al., 2012). This compressional axis suggests the earthquake was not a simple shallow normal- or reverse-faulting event with the strike angle oriented parallel to the trench axis, as is typically seen in many subduction zones (Fig. 1) (U.S. Geological Survey Earthquake

Hazards Program, 2017; Duputel et al., 2012; Dziewonski et al., 1981; Ekström et al., 2012). However, the earthquake produced observable tsunami signals at tide gauges at the northern coast of New Zealand (GeoNet News, 2021), indicating seafloor deformation due to possible shallow slip. All these apparently inconsistent observations (GeoNet, 2021; GeoNet News, 2021) suggest a complex rupture process of the East Cape earthquake, possibly involving multiple faults at different depths.

Although the subduction-related deformation processes in the southern part of the Hikruangi subduction zone have received a lot of scientific attention (e.g., Eberhart-Phillips & Reyners, 1997; Wallace et al., 2009; Mochizuki et al., 2021), the northern segment of Hikurangi margin, where it transitions to the Tonga-Kermadec arc, is less well understood. In region north of East Cape, sporadic deep seismicity (>80-km depth) contrasts with abundant shallow seismicity (<50-km depth) (Dziewonski et al., 1981; Ekström et al., 2012; GeoNet Moment Tensors, 2021; U.S. Geological Survey Earthquake Hazards Program, 2017; GeoNet, 2021). Most of the shallow earthquakes are normal faulting events within the top of the oceanic plate due to trench-normal extensional stress due to slab bending into the trench (Reyners & McGinty, 1999; Henrys et al., 2006; Bassett et al., 2010). With these shallow earthquakes, the plate interface and the surrounding materials have been imaged down to ~20 km depth (Davey et al., 1997; Bell et al., 2010; Bassett et al., 2010, 2016), but the lithospheric structure of the deep slab is poorly resolved. The apparent complex rupture process of the 2021 East Cape earthquake offers a unique opportunity to image the stress regime associated with the deeper subduction process.

Here we show that the rupture process of the 2021 East Cape earthquake involves multiple rupture episodes with a mixture of reverse, strike-slip, and normal faulting mechanisms. These episodes ruptured multiple faults through the subducted oceanic lithosphere at various depths. The earthquake initiated at 70 km depth with an unexpected trench-parallel compressional reverse faulting mechanism, and followed by a slip episode at 30 km depth, which is likely governed by more usual slab-bending trench-normal down-dip extensional stresses. Such a rupture process reflects a heterogeneous stress regime within the subducted slab, in response to a possible geometric change of the slab in depth due to either the subduction of a seamount associated with the Ruatoria debris slide (Lewis et al., 1998; Collot et al., 2001; Lewis et al., 2004), or a sharp change in slab buoyancy at the northern end of the subducting Hikurangi oceanic plateau.

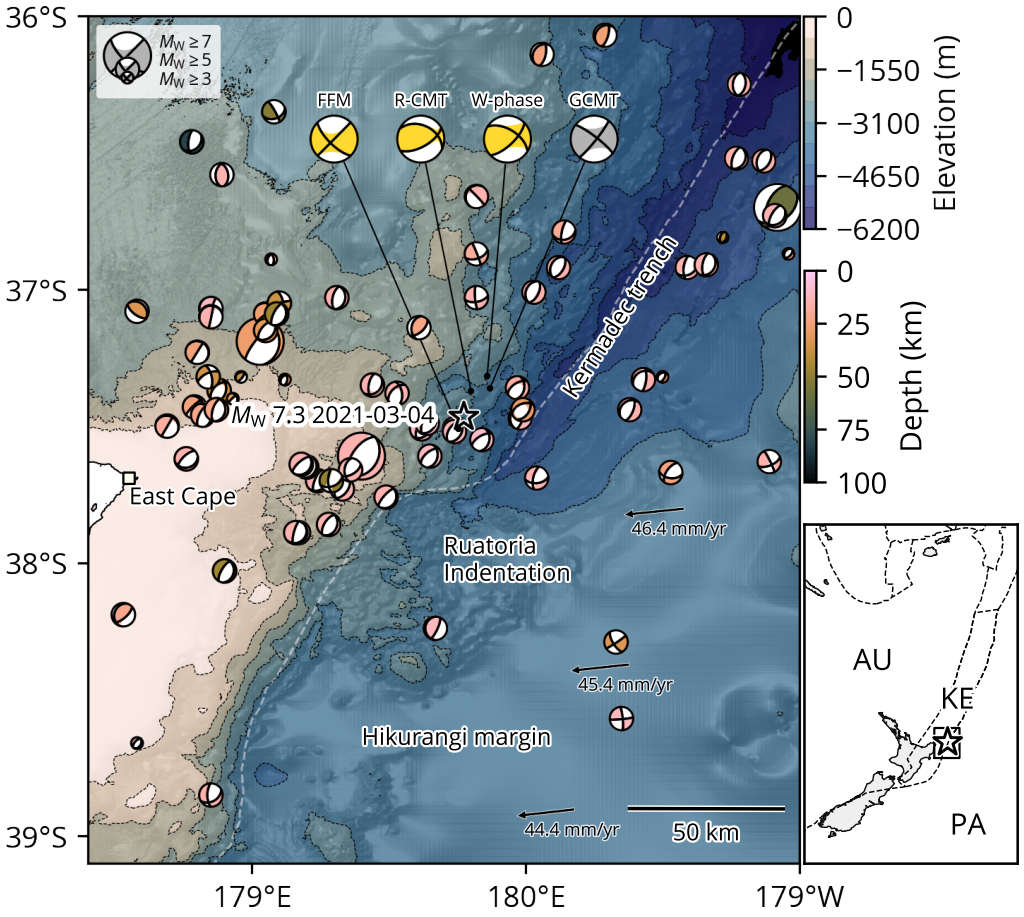

Figure 1. Seismo-tectonic overview of the study region in the north of East Cape, New Zealand. The star shows the relocated hypocenter of the M_W 7.3 2021 East Cape earthquake. Beach balls are the lower-hemisphere stereographic projection of the moment tensor solutions before the 2021 East Cape earthquake, colored by depth (Dziewonski et al., 1981; Ekström et al., 2012). Yellow beach balls are the moment tensor solutions for the 2021 East Cape earthquake obtained by this study (FFM; Finite-fault model, R-CMT; regional centroid moment tensor, *W*-phase; *W*-phase moment tensor). Background contours display the bathymetry (Mitchell et al., 2012). The arrows show the relative plate motions with the convergence rate of the Pacific plate (PA) towards the fixed Australian plate (AU) (DeMets et al., 2010). The dashed line gives the approximate location of the subduction trench (e.g., Bassett et al., 2010). The right map shows the wider setting of the study region. The rectangle shows the area of the left map. The star marks the epicenter. The dashed lines are the plate boundaries (Bird, 2003) between the Pacific (PA), the Australian (AU) and the Kermadec (KE) plates.

2 Hypocenter, aftershock relocation, and initial source estimates

We first determined the hypocenter of the East Cape earthquake by non-linear inversion of *P*- and *S*-wave arrival times at regional distances using a 1D velocity model appropriate for the region north of East Cape (Text S1; Fig. S1). Our relocated epicenter lies along the trench axis, and is within 10 km of the GeoNet solution (GeoNet, 2021), and ~35 km ENE of the U.S. Geological Survey National Earthquake Information Center (USGS-NEIC) solution (U.S. Geological Survey Earthquake Hazards Program, 2017) which is consistent with the USGS-NEIC epicenters being systematically shifted to the down-dip direction in subduction zones (e.g., Ye et al., 2017). Our maximum-likelihood hypocenter depth is 72 km. Although this hypocenter depth may be thought to be inherently uncertain due to the sub-optimal station coverage, it provides an initial hypothesis for testing our results of the more complex rupture configuration later. If we instead fix our hypocentral depth at the fixed GeoNet/USGS estimates of 10–12 km (GeoNet, 2021; U.S. Geological Survey Earthquake Hazards Program, 2017), the root-mean-square residual of arrival times at the closest stations (<200 km) increases by 0.3 s, suggesting that a shallow depth is less compatible with the observations. However, no depth phases were reported in the International Seismological Centre Bulletin for this earthquake (International Seismological Centre, 2021), presumably due to interference with the long source-time function.

Next, we used the `COMPLOC` package (Lin & Shearer, 2005, 2006) to relocate earthquakes near the mainshock hypocenter. The algorithm uses the source-specific station term (SSST) method to relocate the earthquakes, which can greatly improve the relative locations of nearby events because of implementing empirical corrections to neutralize the 3D velocity effects (Richards-Dinger & Shearer, 2000; Lin & Shearer, 2005). We focus on events occurring from January 1, 2021 to May 1, 2021 near the source region of the 2021 East Cape earthquake as there were few events in the region prior to the earthquake. These events are relocated using both *P*- and *S*-wave phase picks from GeoNet (2021) and a 1D velocity profile taken from the NZW2.2 model (Eberhart-Phillips et al., 2010, 2020). We selected the L1-norm as the traveltime-residual misfit measure, and obtained locations for 3484 events (Fig. S2). We find that the distribution of aftershocks from one week after the mainshock (1486 events) is spread across the whole lithosphere, from the seafloor down to ~100 km in depth. We notice several peaks of the large uncertainty in the shallow (<30 km depth) and deep regions (>50 km depth), which likely relate to the discontinuities in the velocity model. However, the widespread seismicity across the whole lithosphere remains a persistent pattern. In particular, the deep aftershocks corroborate our deep mainshock hypocen-

ter hypothesis, and the aftershock distribution indicates a possible multi-fault rupture process of the East Cape earthquake.

Using a Bayesian bootstrapping centroid-moment tensor (CMT) inversion of low-frequency (2.0–8.5 mHz) teleseismic waveforms for a single-point source (Text S2), we find a mean centroid depth of 53 km, with a centroid position shifted 18 km NNE of our relocated epicenter, and time shift from the origin time of +5 s (Fig. S3). However, the CMT solution has a large non-double couple component (DC=15%). Such a low DC component is likely caused by geometric complexities of the earthquake that may involve multiple faults within the subducted Pacific plate near the Hikurangi trench.

Finally, to test the hypothesised rupture complexity, we investigated the rupture process of the earthquake with a multi-point centroid moment tensor (R-CMT) inversion method using regional seismic waveforms (Text S3; Figs. S4 to S6). The approach can resolve the first-order features of a complex rupture with few assumptions. Due to the low-velocity accretionary wedge, the later part of the <25 s period surface waves on the horizontal components at stations within ~400 km epicentral distance are poorly fit (Figs. S5 and S6) due to basin resonance effects (Kaneko et al., 2019). We find that the East Cape event can be best explained by two sub-events, with the largest sub-event (M_W ~7.3) at 50–70 km depth occurring 8–10 s after the origin time, and the second sub-event at 7–12 km depth and 6–8 s after the first sub-event. The second sub-event significantly increases waveform variance reduction by 16–23%. The first sub-event has an oblique-reverse mechanism. Conversely, the second sub-event has a normal faulting mechanism. The shallow aftershock lineation (10–30 km depth) dips to the west (Fig. S2), which suggests the fault plane is likely oriented along the trench axis. Overall, our R-CMT solution corroborates a complex rupture scenario involving at least two sub-events separated by ~40 km in depth: one in the top of the Pacific plate, the other deep within the slab.

3 Intermittent complex multiple rupture episodes with various focal mechanisms

To better understand the rupture development, we applied a finite-fault potency-density inversion method (Shimizu et al., 2020) to estimate the rupture evolution of the 2021 East Cape earthquake (Text S4). The method can flexibly accommodate multiple faults with different geometries rupturing during the same event, which are inferred from the spatiotemporal distribution of five-basis double-couple components of the potency-density tensors (Kikuchi & Kanamori, 1991; Ampuero & Dahlen, 2005). In our inversion formulation, the model parameters are objectively determined by minimizing Akaike's Bayesian Information Criterion (ABIC) (Akaike, 1980; Yabuki & Matsu'ura,

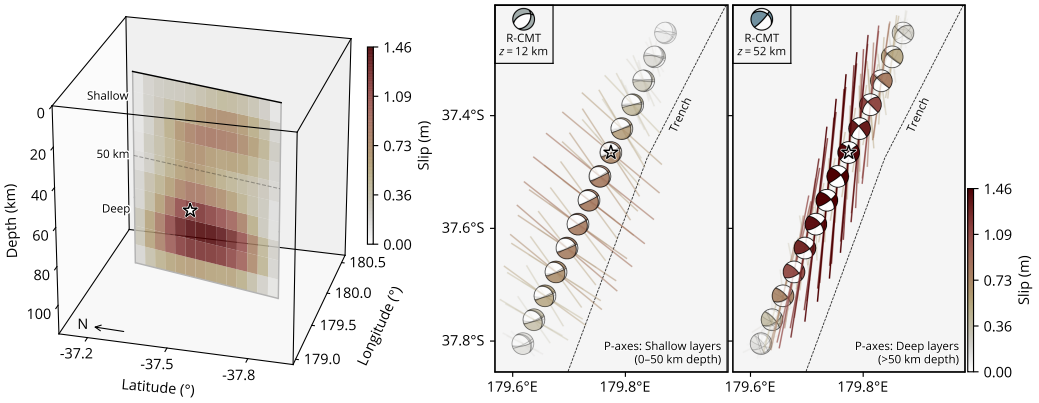

Figure 2. Static slip distribution. The left panel shows the total slip distribution in a 3D view, viewed from the south-west. The star represents our hypocenter. The black line shows the top of the model fault. The right panels show the map view of the slip distribution from shallow (<50 km) and deep depths (≥50 km), with beach balls representing double-couple components (Fig. S7), and corresponding P-axis azimuths (bars scaled by slip). The P-axis azimuth is extracted from the resultant double-couple solution for each sub-fault, which is represented by a lower-hemisphere stereographic projection. We show the beach balls from the slip patch corresponding to the fault element with the maximum slip within each given depth range. The inset shows the corresponding R-CMT solutions annotated with their depths (z). The dashed line is the subduction trench (Bird, 2003).

1992), and we do not adopt non-negative constraints for slip vectors. Such a procedure can effectively prevent over- or under-smoothing of the source model as theoretically shown in Fukuda and Johnson (2008). Particularly, we flexibly solve the potency density in a finite-fault domain instead of regularizing the model with possible inaccurate subjective assumptions (e.g., positivity constraints, and the prescribed fault geometry). The method has proven effective at resolving complex earthquake ruptures in a variety of tectonic settings (Shimizu et al., 2020, 2021; Okuwaki et al., 2020; Hicks et al., 2020; Tadapansawut et al., 2021; Yamashita et al., 2021). In practice, we parametrize a 2D vertical model domain along a 200° strike extending from 7- to 107-km depth with a total of 140 source elements (sub-faults) (Fig. 2). This parameterization is guided by the observed cluster of the near-trench-parallel aftershocks (Fig. S2). Although it is difficult to resolve the absolute locations of slip surfaces due to insufficient spatial resolution of the teleseismic body waves used in our finite-fault modeling, in the 2D model domain, we solve the fault-normal and shear-slip vectors at each source element, which are independent of the model domain geometry. In other words, we solve for distributed sources in the model domain that may have any type of faulting mechanism required by the data. The model domain therefore allows multiple faulting episodes of the earthquake and does not necessarily indicate a single fault plane cutting through the lithosphere in a continuous rupture. Our preferred slip model suggests that the earthquake initiated at 72 km depth (Fig. S12) corroborating the relocated hypocenter and the R-CMT solution.

Our preferred finite-fault model suggests that most slip occurred at 55 to 100 km depth and ~15 km south of the hypocenter, releasing 69% of the total moment (Fig. 2). Another patch of slip is observed at 20–40 km depth, much shallower than the hypocentral depth and comprising 31% of the total moment. The deeper slip is dominated by an oblique strike-slip faulting mechanism. The shallow slip involves a mixture of normal and strike-slip faulting mechanisms. The finite-fault model leads to a moment estimate of 1.7×10^{20} Nm (M_{W} 7.4). We evaluated the robustness and uncertainty of the finite-fault model by performing synthetic tests (Fig. S13). The result shows that both the slip pattern and the variation of faulting mechanism in the model domain are well reproduced. We will discuss in detail in a later section, but the focal mechanisms of the shallow and deep domains agree with the R-CMT solutions (Fig. 2), which show shallow normal faulting with the likely fault plane orienting along the trench axis and deep reverse faulting with the compressional axis orienting along the trench axis.

The rupture process of the East Cape earthquake involved at least four distinct episodes (E1 to E4) with the deep- and shallow-slips corresponding to different faulting types. The earthquake initiated as a reverse faulting with a strike-slip component for the first 5 s (E1, Fig. 3). The rupture then propagated towards the south at 60–100 km depth, releasing 20% of the total moment and lasting for about 5 s (E2, Fig. 3). This episode was dominated by thrust faulting. The third episode (E3) simultaneously ruptured several fault patches from 10 to 15 s, including a shallow patch at ~25 km depth and a deep patch ~70 km depth (Fig. 3). The shallow part of E3 ruptured with a normal faulting mechanism, while the deep patch of E3 had a strike-slip mechanism. The last major episode (E4) ruptured a fault patch beneath the hypocenter for about 5 s with a dominant strike slip focal mechanism (Fig. 3). The remaining 26% of the total moment was released by slips at both shallow and deep regions, and the earthquake lasted for about ~30 s.

The four rupture episodes are compact in size and are spatially distinct from each other. Given the varying focal mechanisms, the chaotic episodes likely do not result from the same continuous rupture front, but more likely represent segmented slip on different faults that may have interacted with, and triggered, each other.

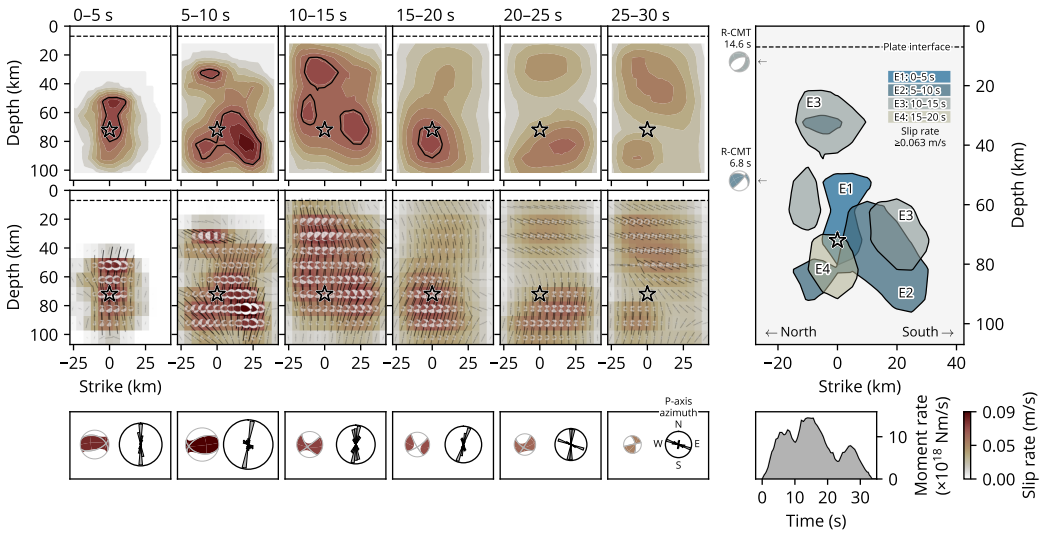

Figure 3. Slip evolution. The left panels show the cross sections of the spatio-temporal distribution of slip rate and the resultant moment-rate tensor solution, given in 5 s long windows. The star represents the hypocenter. The dashed line is the top of the subducting plate (Bassett et al., 2010). The black contour highlights faster slip rates (≥0.063 m/s; ≥70% of maximum slip rate). The centroid moment tensor for each time window is shown at the bottom, together with the rose diagram of P-axis azimuths weighted by slip rate. All the beach balls of the moment-tensor solution are represented as a lower-hemisphere stereographic projection, not rotated according to the model geometry, but in map view. The right panel summarizes the slip-rate evolution. The color for each episode (E1 to E4) corresponds to the time window. The minor slip-rate events within the final two time windows (20–30 s) are not slipping fast enough to plot a contour on the right panel. R-CMT solutions are also shown at the corresponding depths, with their time shift given relative to the hypocentral time. The right-bottom inset is the total moment-rate function from the finite-fault model.

4 Intraslab stress rotation in depth

The source process of the 2021 East Cape earthquake is characterized by spatiotemporally disconnected, multiple episodes rupturing from deep to shallow within the subducted slab (Fig. 2). For the shallow slip episode, its focal mechanism shows a mixture of the normal faulting with a strike-slip component. The general trend of the aftershock distribution (Fig. S2) suggests that the fault plane striking toward the northeast-southwest direction likely ruptured during the later phase of the earthquake. Although the limited station azimuth coverage could cause an artificially elongated aftershock distribution, the major axis of the uncertainty ellipse of the mainshock relocation, which shares the similar station coverage, is oriented W-E rather than SW-NE (Fig. S1). It is noteworthy that some aftershocks (U.S. Geological Survey Earthquake Hazards Program, 2017; Dziewonski et al., 1981; Ekström et al., 2012; GeoNet Moment Tensors, 2021) share similar focal mechanisms to the shallow rupture episode (Fig. S8). Given the near-trench location of the East Cape earthquake, there is some ambiguity regarding the exact faulting configuration. However, the aftershock distribution indicates that the shallow slip episode likely ruptured a normal fault within the downgoing plate. Additionally, in the absence of clear shallow slip with a reverse-faulting mechanism, this normal faulting episode likely caused the observed tsunami.

The varying focal-mechanisms of the four slip episodes (E1–E4) show the compressional stress orientation (the P-axis orientation) of the East Cape earthquake rotated from the northwest-southeast direction to the north-south direction with a gap in slip and approximate stress transition depth at ~50 km (Figs. 2 and 3). The normal faulting of the shallow slip episodes striking toward the northeast-southwest direction agrees well with the extensional stress in the upper part of the subducted plate due to the expected plate bending and pulling process (e.g., Astiz et al., 1988; Ammon et al., 2008; Craig et al., 2014; Romeo & Álvarez-Gómez, 2018; Sandiford et al., 2020). Such a bending process seems to have caused most of the background seismicity in this region, which has predominant normal faulting mechanisms (Fig. 1; Reyners & McGinty, 1999; Bassett et al., 2010). If the deep slip at 50–100-km depth during the East Cape earthquake was driven by the same bending-related process, we would expect a trench-normal P-axis orientation, which is typical for similar events at other subduction zones, where deep trench-parallel reverse faulting is observed (e.g., Okada & Hasegawa, 2003; Ohta et al., 2011; Ye et al., 2012; Todd & Lay, 2013; Ye et al., 2021). However, the deep slip patches of the East Cape earthquake (E1 and E2, and R-CMT Sub-event 1) have oblique-thrusting mechanisms, resulting in a trench-parallel com-

277 pression. This perplexing P-axis orientation indicates an additional regional factor that
278 may have modulated the rupture process of the East Cape earthquake.

279 The interactivity between various faulting episodes is a puzzling part of the East
280 Cape earthquake. Subduction zone earthquakes may involve multiple disconnected
281 subevents with different faulting types that can trigger and interact with each other
282 (Ammon et al., 2008; Lay et al., 2013; Hicks & Rietbrock, 2015; Lay et al., 2020). For
283 the East Cape earthquake, our preferred finite-fault model does not show a contin-
284 uous rupturing path from the deep to shallow episodes (Figs. 2 and 3). The shallow
285 rupture E3 is separated by ~40 km from the deep episodes and started ~5 s later (Fig.
286 3), suggesting an apparent rupture speed of ~8 km/s if the rupture was continuous.
287 Such a rupture speed would be close to the local *P*-wave speed (Table S1), which is
288 unlikely. More likely, slip episodes E1 and E2 triggered the following shallow episode
289 E3 due to either the static and/or dynamic stress change from the initial deep rup-
290 ture. A stress transition or strength contrast within the slab can work as an inhomo-
291 geneous barrier (Das & Aki, 1977; Aki, 1979) to smooth propagation from deep to shal-
292 low rupture during the East Cape earthquake. Therefore, the rupture evolution of the
293 earthquake may have developed as discontinuous jumps by means of stress trigger-
294 ing (Miyazawa & Mori, 2005; Sleep & Ma, 2008; Fischer, Sammis, et al., 2008; Fischer,
295 Peng, & Sammis, 2008) across the apparent stress/strength barrier between the deep
296 and shallow rupture areas.

297 Large intraplate earthquakes within the downgoing plate in subduction zones
298 are typically caused either by the down-dip bending and unbending of the slab (e.g.,
299 Astiz et al., 1988; Craig et al., 2014; Sandiford et al., 2020), the reactivation of ma-
300 jor oceanic fabrics, including fracture zones (e.g., Abercrombie et al., 2003; Meng et
301 al., 2012; Yue et al., 2012), or the tearing of the slab (e.g., Tanioka et al., 1995). How-
302 ever, the orientation and rupture complexity of the 2021 East Cape event deviates from
303 these typical events. Two events with apparently similar deep trench-parallel com-
304 pression in the slab include 2003 M_W 7.9 Enggano and 2009 M_W 7.6 Padang earth-
305 quakes, offshore Sumatra (Abercrombie et al., 2003; Wiseman et al., 2012). However,
306 these events likely ruptured pre-existing fabrics in the downgoing plate (Abercrombie
307 et al., 2003), such as fracture zones (Wiseman et al., 2012). Both earthquakes poten-
308 tially represent the continuation of the diffuse deformation within the Wharton basin,
309 and both consistently ruptured orthogonal fabrics toward the top of the downgoing
310 plate both updip and downdip from the trench, where highly oblique convergence in-
311 herently causes a rotated state of the stress in the slab. In contrast, the 2021 East Cape
312 earthquake, which occurred deeper beneath the top of the slab, does not align with

the expected oceanic fabric, and is not obviously part of a wider, plate-scale, deformation field, where there is no obvious oblique convergence nor are fracture zones of an orientation consistent with the observed mechanisms subducted (Fig. 1). Instead, the rupture processes may represent a unique case, highlighting a different type of stress transition within the subducted slab.

5 A contorted slab structure due to slab buoyancy variations?

A key question is why does this part of the Hikurangi subduction zone exhibit an atypical stress regime, as manifested in the rupture process of the 2021 East Cape earthquake? Slab models of this region (Hayes, 2018; Hayes et al., 2018; Williams et al., 2013) show a homogeneous planar structure (Fig. S9) which would be expected to lead to a trench-normal compression in the deeper part of the slab. However, these slab models are poorly constrained near the East Cape earthquake, largely because of a lack of plate interface thrust earthquakes in the region (Fig. 1). The rupture process of the East Cape earthquake therefore potentially offers new insight into the local slab structure.

One possible explanation is that the slab surface warps downward north of the hypocenter, forming a depression at the plate interface (Fig. 4). The warping is likely a response to the buoyancy gradients in the subducting plate, which allows the less buoyant parts of the slab to sink more rapidly than the buoyant parts. The internal stress field from such a slab topology would be complex, leading to strong 3-D stress rotations around the localized downwarp in a manner as shown in the 2021 East Cape earthquake (Fig. 2). One contribution to the buoyancy gradients might be the subduction of a large-scale seamount. About 30 km south-west from the epicenter, the Quaternary Ruatoria seamount was obliquely subducted at the margin (Lewis et al., 1998; Collot et al., 2001; Lewis et al., 2004), forming the characteristic bathymetry of the Ruatoria indentation (Fig. 1). The Ruatoria seamount could deflect and bend the slab, causing the intraslab stress state to rotate from trench-normal compression to trench-parallel compression across the hypocentral area. Numerical models of slab stress in the presence of subducted buoyant features in the oceanic plate support such a stress rotation and lateral spreading mechanism (e.g., Mason et al., 2010). Trench-parallel compression has also been seen in other parts in the Hikurangi subduction zone, for example, McGinty et al. (2000) observed the strike-slip seismicity with trench-parallel compression at depths 40–80 km offshore from the Raukumara Peninsula. Although these earthquakes beneath the Raukumara Peninsula should reflect the stress state once the plate is already subducted, rather than at the trench region which is

where the 2021 East Cape earthquake illuminates, it is possible they reflect stress heterogeneity due to pervasive seamount subduction along the northern Hikurangi subduction zone (Barker et al., 2009).

An alternative explanation may arise from the location of the East Cape earthquake with respect to the transition between the Kermadec trench and Hikurangi margin, marked by the edge of the Hikurangi plateau, which is represented by a clear bathymetric scarp running along its northern boundary (Davy & Collot, 2000). This transition from the subduction of normal oceanic lithosphere to the north, to the subduction of the thickened oceanic crust associated with the igneous Hikurangi plateau likely leads to a pronounced, short-wavelength flexural warping at the plateaus edge. The superposition of this N-S flexural stress field with the stress field related to the down-dip bending would produce a complex pattern that varies at short-length scales within the subducted slab, and could impact on the rupture process seen in the compound East Cape earthquake. It is noteworthy that in 2001, ~80 km northeast of the 2021 event, there was a M_W 7.1 earthquake deep in the Pacific plate (~60 km depth) showing a reverse faulting mechanism with its P-axis oriented perpendicular to the Kermadec trench (Fig. S8), which was likely driven by conventional trench-normal down-dip compression. This earthquake suggests that flexural warping due to the subducting Hikurangi plateau does not extend this far to the north.

Whilst there have been many studies on the impact of subducting buoyant features on subduction megathrust coupling and interface seismogenesis (e.g., Wang & Bilek, 2011; Nishikawa & Ide, 2014), there have been far fewer studies that have considered their impact on intraslab seismicity. The rarity of deep intraslab earthquakes in the northern Hikurangi subduction zone makes it difficult to distinguish between the seamount and plateau models of stress rotation. However, it is also possible that both features play a concurrent role, with stress rotations superimposed from both.

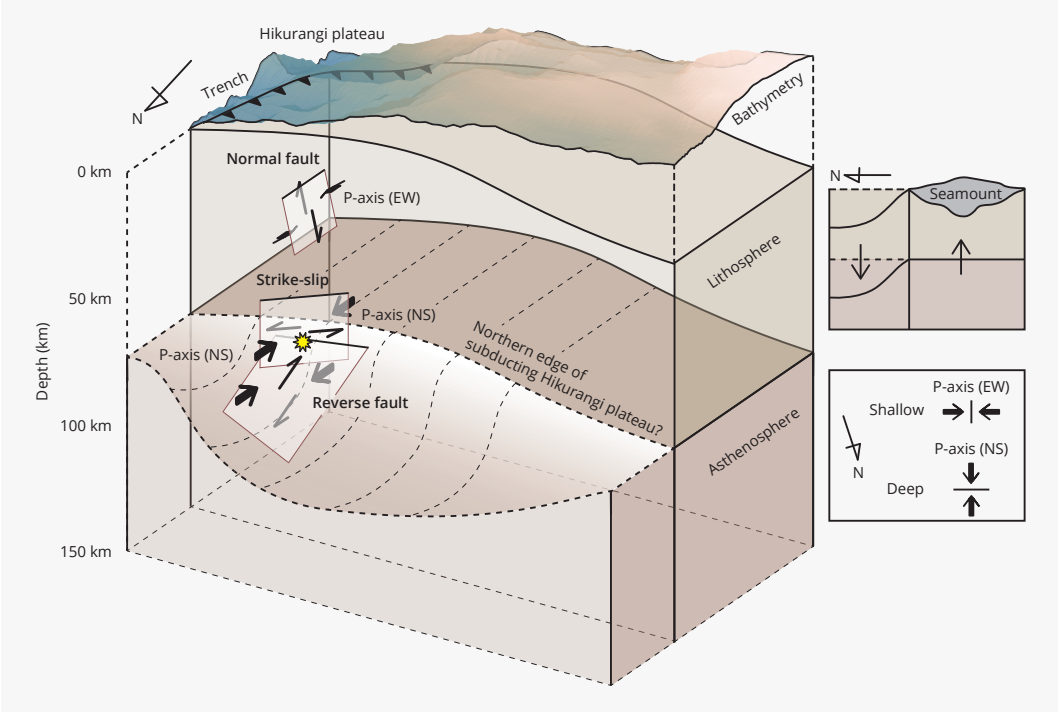

Figure 4. Schematic figure showing the inferred slab geometry, stress regimes and faulting styles based on our observations of the 2021 East Cape earthquake. The yellow marker shows the hypocenter. The arrow shows the compressional axis. The one-side arrow represents the fault motion. The bathymetry is from Mitchell et al. (2012) with its height being exaggerated ×15. The upper right panel is a cross-section with the arrows showing the relative force applied in the slab. The lower right panel shows the compressional axes in a top view.

6 Conclusions

We determined the rupture geometry of the 2021 M_W 7.3 East Cape, New Zealand earthquake using a novel finite-fault inversion technique. Our method does not require a-priori knowledge of the fault geometry and can flexibly resolve complex faulting styles in large earthquakes. Therefore, it can uniquely illuminate the heterogeneous stress state near the earthquake. We show that the East Cape earthquake has at least four rupture episodes and likely ruptured multiple faults with various faulting styles. We find distinct rupture episodes within the shallow (~30 km) and deep (~70 km) parts of the subducted oceanic plate, with distinct mechanisms of normal and a mixture of strike-slip and reverse faulting, respectively. The deep and shallow episodes likely reflect components of a flexural stress field, separated by a low-stress barrier in the middle of the plate. The rotation of P-axes suggests that the intraplate stress state is locally rotated from trench-normal compression to trench-parallel compression. Such a stress rotation in depth requires the slab geometry to change sharply, which may have been induced by a subducted seamount or the additional buoyancy of the Hikurangi plateau. Our study suggests that understanding the generation of intermediate and deep intraslab seismicity requires a detailed treatment of localized variations in slab geometry caused by the subduction of heterogeneous features, such as ocean plateaus and seamounts.

Acknowledgments

We thank the editor Dr. Germán Prieto, the associate editor Dr. Ake Fagereng, the reviewer Dr. Emily Warren-Smith, and the anonymous reviewer for their evaluations and constructive suggestions. We thank Lingsen Meng, Han Bao, Baoning Wu, Richard G. Davy, Lior Suchoy, Fangqin Chen, Rhodri Davies, Tian Feng, Yuqing Xie, Liuwei Xu and Tong Zhou for the discussions. We are also grateful to John Ristau for discussions on the original GeoNet moment tensor solutions. TJC was supported in this work by the Royal Society under URF\R1\180088. COMET is the NERC Centre for the Observation and Modelling of Earthquakes, Volcanoes and Tectonics, a partnership between UK Universities and the British Geological Survey. This work was supported by the Grant-in-Aid for Scientific Research (C) 19K04030. The facilities of IRIS Data Services, and specifically the IRIS Data Management Center, were used for access to waveforms, related metadata, and/or derived products used in this study. IRIS Data Services are funded through the Seismological Facilities for the Advancement of Geoscience (SAGE) Award of the National Science Foundation under Cooperative Support Agreement EAR-1851048. We also thank the GeoNet data centre for making their continuous broadband and strong motion seismic data openly available. The authors declare no conflicts of interest relevant to this study.

Data Availability Statement

All the materials presented in this paper are archived and available at https://doi.org/10.5281/zenodo.5386179. All seismic data were downloaded through the IRIS Wilber 3 system (https://ds.iris.edu/wilber3/find_event) or IRIS Web Services (https://service.iris.edu), including the following seismic networks: the GT (Global Telemetered Seismograph Network (USAF/USGS); Albuquerque Seismological Laboratory (ASL)/USGS, 1993); the IC (New China Digital Seismograph Network; Albuquerque Seismological Laboratory (ASL)/USGS, 1992); the IU (Global Seismograph Network (GSN - IRIS/USGS); Albuquerque Seismological Laboratory (ASL)/USGS, 1988); the GE (GEOFON Seismic Network; GEOFON Data Centre, 1993); the AU (Australian National Seismograph Network (ANSN); Geoscience Australia (GA), 1994); the HK (Hong Kong Seismograph Network; Hong Kong Observatory, 2009); the G (GEOSCOPE; Institut De Physique Du Globe De Paris (IPGP) & Ecole Et Observatoire Des Sciences De La Terre De Strasbourg (EOST), 1982); the NZ (New Zealand National Seismograph Network; Institute of Geological & Nuclear Sciences Ltd (GNS New Zealand), 1988; Petersen et al., 2011); the AI (Antarctic Seismographic Argentinean Italian Network - OGS; Istituto Nazionale Di Oceanografia E Di Geofisica Sperimentale, 1992); the II (IRIS/IDA Seismic Network;

Scripps Institution Of Oceanography, 1986); the C (Chilean National Seismic Network; Universidad de Chile Dept de Geofisica (DGF UChile Chile), 1991); the PS (Pacific21 (ERI/STA); University of Tokyo Earthquake Research Institute (Todai ERI Japan), 1989). We used ObsPy (Beyreuther et al., 2010, version 1.1.0; https://doi.org/10.5281/zenodo.165135), Pyrocko (The Pyrocko Developers, 2017, https://pyrocko.org/), matplotlib (Hunter, 2007, version 3.0.3; https://doi.org/10.5281/zenodo.2577644), Generic Mapping Tools (Wessel & Luis, 2017, version 6.1.0; http://doi.org/10.5281/zenodo.3924517); and Scientific colour maps (Crameri, 2018; Crameri et al., 2020, version 6.0.4; http://doi.org/10.5281/zenodo.4153113) for data processing and visualisation. The `NonLinLoc` software used for hypocenter relocation is available at http://alomax.free.fr/nlloc/. The `Grond` software (Heimann et al., 2018) used for *W*-phase CMT inversion is available at https://pyrocko.org/grond/docs/current/. The `ISOLA` software used for R-CMT inversion is available at http://seismo.geology.upatras.gr/isola/. The `COMPLOC` earthquake location package (Lin & Shearer, 2005, 2006) for aftershock relocation is available at https://sites.google.com/view/guoqing-lin/products/comploc.

References

Abercrombie, R. E., Antolik, M., & Ekström, G. (2003). The June 2000 Mw 7.9 earthquakes south of Sumatra: Deformation in the India-Australia Plate . *J. Geophys. Res. Solid Earth*, *108*(B1), 2018. doi:10.1029/2001jb000674

Akaike, H. (1980). Likelihood and the Bayes procedure. *Trab. Estad. Y Investig. Oper.*, *31*(1), 143–166. Retrieved from https://doi.org/10.1007/BF02888350 doi:10.1007/BF02888350

Aki, K. (1979). Characterization of barriers on an earthquake fault. *J. Geophys. Res.*, *84*(B11), 6140. doi:10.1029/JB084iB11p06140

Albuquerque Seismological Laboratory (ASL)/USGS. (1988). *Global Seismograph Network (GSN - IRIS/USGS).* International Federation of Digital Seismograph Networks. doi:10.7914/SN/IU

Albuquerque Seismological Laboratory (ASL)/USGS. (1992). *New China Digital Seismograph Network.* International Federation of Digital Seismograph Networks. doi:10.7914/SN/IC

Albuquerque Seismological Laboratory (ASL)/USGS. (1993). *Global Telemetered Seismograph Network (USAF/USGS).* International Federation of Digital Seismograph Networks. Retrieved from http://www.fdsn.org/doi/10.7914/SN/GT doi:10.7914/SN/GT

Ammon, C. J., Kanamori, H., & Lay, T. (2008). A great earthquake doublet and seismic stress transfer cycle in the central Kuril islands. *Nature*, *451*(7178), 561–

565. doi:10.1038/nature06521

Ampuero, J.-P., & Dahlen, F. A. (2005). Ambiguity of the Moment Tensor. *Bull. Seismol. Soc. Am.*, *95*(2), 390–400. doi:10.1785/0120040103

Arai, R., Takahashi, T., Kodaira, S., Kaiho, Y., Nakanishi, A., Fujie, G., ... Kaneda, Y. (2016). Structure of the tsunamigenic plate boundary and low-frequency earthquakes in the southern Ryukyu Trench. *Nat. Commun.*, *7*, 1–7. doi:10.1038/ncomms12255

Astiz, L., Lay, T., & Kanamori, H. (1988). Large intermediate-depth earthquakes and the subduction process. *Phys. Earth Planet. Inter.*, *53*(1-2), 80–166. doi:10.1016/0031-9201(88)90138-0

Avouac, J. P., Ayoub, F., Wei, S., Ampuero, J. P., Meng, L., Leprince, S., ... Helmberger, D. (2014). The 2013, Mw 7.7 Balochistan earthquake, energetic strike-slip reactivation of a thrust fault. *Earth Planet. Sci. Lett.*, *391*, 128–134. doi:10.1016/j.epsl.2014.01.036

Barker, D. H., Sutherland, R., Henrys, S., & Bannister, S. (2009). Geometry of the Hikurangi subduction thrust and upper plate, North Island, New Zealand. *Geochemistry, Geophys. Geosystems*, *10*(2). doi:10.1029/2008GC002153

Bassett, D., Kopp, H., Sutherland, R., Henrys, S., Watts, A. B., Timm, C., ... Ronde, C. E. J. (2016). Crustal structure of the Kermadec arc from MANGO seismic refraction profiles. *J. Geophys. Res. Solid Earth*, *121*(10), 7514–7546. doi:10.1002/2016JB013194

Bassett, D., Sutherland, R., Henrys, S., Stern, T., Scherwath, M., Benson, A., ... Henderson, M. (2010). Three-dimensional velocity structure of the northern Hikurangi margin, Raukumara, New Zealand: Implications for the growth of continental crust by subduction erosion and tectonic underplating. *Geochemistry, Geophys. Geosystems*, *11*(10). doi:10.1029/2010GC003137

Bell, R., Sutherland, R., Barker, D. H., Henrys, S., Bannister, S., Wallace, L., & Beavan, J. (2010). Seismic reflection character of the Hikurangi subduction interface, New Zealand, in the region of repeated Gisborne slow slip events. *Geophys. J. Int.*, *180*(1), 34–48. doi:10.1111/j.1365-246X.2009.04401.x

Beyreuther, M., Barsch, R., Krischer, L., Megies, T., Behr, Y., & Wassermann, J. (2010). ObsPy: A Python Toolbox for Seismology. *Seismol. Res. Lett.*, *81*(3), 530–533. doi:10.1785/gssrl.81.3.530

Bird, P. (2003). An updated digital model of plate boundaries. *Geochemistry, Geophys. Geosystems*, *4*(3), 1105. doi:10.1029/2001GC000252

Collot, J. Y., Delteil, J., Lewis, K. B., Davy, B., Lamarche, G., Audru, J. C., ... Uruski, C. (1996). From oblique subduction to intra-continental transpression:

Structures of the southern Kermadec-Hikurangi margin from multibeam bathymetry, side-scan sonar and seismic reflection. *Mar. Geophys. Res.*, *18*(2-4), 357–381. doi:10.1007/BF00286085

Collot, J. Y., Lewis, K., Lamarche, G., & Lallemand, S. (2001). The giant Ruatoria debris avalanche on the northern Hikurangi margin, New Zealand: Result of oblique seamount subduction. *J. Geophys. Res. Solid Earth*, *106*(B9), 19271–19297. doi:10.1029/2001jb900004

Craig, T. J., Copley, A., & Jackson, J. (2014). A reassessment of outer-rise seismicity and its implications for the mechanics of oceanic lithosphere. *Geophys. J. Int.*, *197*(1), 63–89. doi:10.1093/gji/ggu013

Crameri, F. (2018). Geodynamic diagnostics, scientific visualisation and StagLab 3.0. *Geosci. Model Dev.*, *11*(6), 2541–2562. doi:10.5194/gmd-11-2541-2018

Crameri, F., Shephard, G. E., & Heron, P. J. (2020). The misuse of colour in science communication. *Nat. Commun.*, *11*(1), 5444. doi:10.1038/s41467-020-19160-7

Das, S., & Aki, K. (1977). Fault plane with barriers: A versatile earthquake model. *J. Geophys. Res.*, *82*(36), 5658–5670. doi:10.1029/JB082i036p05658

Dascher-Cousineau, K., Brodsky, E. E., Lay, T., & Goebel, T. H. W. (2020). What Controls Variations in Aftershock Productivity? *J. Geophys. Res. Solid Earth*, *125*(2), e2019JB018111. doi:10.1029/2019JB018111

Davey, F. J., Henrys, S., & Lodolo, E. (1997). A seismic crustal section across the East Cape convergent margin, New Zealand. *Tectonophysics*, *269*(3-4), 199–215. doi:10.1016/S0040-1951(96)00165-5

Davy, B., & Collot, J. Y. (2000). The Rapuhia Scarp (northern Hikurangi Plateau) - Its nature and subduction effects on the Kermadec Trench. *Tectonophysics*, *328*(3-4), 269–295. doi:10.1016/S0040-1951(00)00211-0

DeMets, C., Gordon, R. G., & Argus, D. F. (2010). Geologically current plate motions. *Geophys. J. Int.*, *181*(1), 1–80. doi:10.1111/j.1365-246X.2009.04491.x

Duputel, Z., Rivera, L., Kanamori, H., & Hayes, G. (2012). W phase source inversion for moderate to large earthquakes (1990-2010). *Geophys. J. Int.*, *189*(2), 1125–1147. doi:10.1111/j.1365-246X.2012.05419.x

Dziewonski, A. M., Chou, T.-A., & Woodhouse, J. H. (1981). Determination of earthquake source parameters from waveform data for studies of global and regional seismicity. *J. Geophys. Res. Solid Earth*, *86*(B4), 2825–2852. doi:10.1029/JB086iB04p02825

Eberhart-Phillips, D., Bannister, S., Reyners, M., & Henrys, S. (2020). *New Zealand Wide model 2.2 seismic velocity and Qs and Qp models for New Zealand*. Zenodo.

539 doi:10.5281/zenodo.3779523
540 Eberhart-Phillips, D., & Reyners, M. (1997). Continental subduction and three-
541 dimensional crustal structure: The northern South Island, New Zealand. *J.*
542 *Geophys. Res. B Solid Earth*, *102*(6), 11843–11861. doi:10.1029/96jb03555
543 Eberhart-Phillips, D., Reyners, M., Bannister, S., Chadwick, M., & Ellis, S. (2010).
544 Establishing a versatile 3-D seismic velocity model for New Zealand. *Seismol.*
545 *Res. Lett.*, *81*(6), 992–1000. doi:10.1785/gssrl.81.6.992
546 Ekström, G., Nettles, M., & Dziewoński, A. (2012). The global CMT project
547 2004–2010: Centroid-moment tensors for 13,017 earthquakes. *Phys. Earth*
548 *Planet. Inter.*, *200-201*, 1–9. doi:10.1016/j.pepi.2012.04.002
549 Elliott, J. R., Jolivet, R., Gonzalez, P. J., Avouac, J. P., Hollingsworth, J., Searle, M. P.,
550 & Stevens, V. L. (2016). Himalayan megathrust geometry and relation to
551 topography revealed by the Gorkha earthquake. *Nat. Geosci.*, *9*(2), 174–180.
552 doi:10.1038/ngeo2623
553 Fischer, A. D., Peng, Z., & Sammis, C. G. (2008). Dynamic triggering of high-
554 frequency bursts by strong motions during the 2004 Parkfield earthquake
555 sequence. *Geophys. Res. Lett.*, *35*(12), L12305. doi:10.1029/2008GL033905
556 Fischer, A. D., Sammis, C. G., Chen, Y., & Teng, T.-L. (2008). Dynamic
557 Triggering by Strong-Motion P and S Waves: Evidence from the 1999
558 Chi-Chi, Taiwan, Earthquake. *Bull. Seismol. Soc. Am.*, *98*(2), 580–592.
559 doi:10.1785/0120070155
560 Floyd, M. A., Walters, R. J., Elliott, J. R., Funning, G. J., Svarc, J. L., Murray, J. R., ...
561 Wright, T. J. (2016). Spatial variations in fault friction related to lithology
562 from rupture and afterslip of the 2014 South Napa, California, earthquake.
563 *Geophys. Res. Lett.*, *43*(13), 6808–6816. doi:10.1002/2016GL069428
564 Fukuda, J., & Johnson, K. M. (2008). A fully Bayesian inversion for spatial distribu-
565 tion of fault slip with objective smoothing. *Bull. Seismol. Soc. Am.*, *98*(3), 1128–
566 1146. doi:10.1785/0120070194
567 GEOFON Data Centre. (1993). *GEOFON Seismic Network.* Deutsches Geo-
568 ForschungsZentrum GFZ. doi:10.14470/TR560404
569 GeoNet. (2021). *GeoNet Earthquake Catalog.* Retrieved from https://www.geonet.org
570 .nz/data/types/eq_catalogue
571 GeoNet Moment Tensors. (2021). *GeoNet Moment Tensors.* Retrieved from https://
572 github.com/GeoNet/data/tree/main/moment-tensor
573 GeoNet News. (2021). *Friday 5 March Tsunami: What happened and*
574 *what did you see?* Retrieved from https://www.geonet.org.nz/news/
575 1gvqV0oHGIULbydSQD8W1Y

Geoscience Australia (GA). (1994). *Australian National Seismograph Network (ANSN).* Retrieved from https://www.fdsn.org/networks/detail/AU/

Gomberg, J., & Bodin, P. (2021). The Productivity of Cascadia Aftershock Sequences. *Bull. Seismol. Soc. Am.*, *111*(3), 1–14. doi:10.1785/0120200344

Hamling, I. J., Hreinsdóttir, S., Clark, K., Elliott, J., Liang, C., Fielding, E., … Stirling, M. (2017). Complex multifault rupture during the 2016 Mw 7.8 Kaikōura earthquake, New Zealand. *Science*, *356*(6334). doi:10.1126/science.aam7194

Hayes, G. P. (2018). *Slab2 - A Comprehensive Subduction Zone Geometry Model: U.S. Geological Survey data release.* doi:10.5066/F7PV6JNV

Hayes, G. P., Moore, G. L., Portner, D. E., Hearne, M., Flamme, H., Furtney, M., & Smoczyk, G. M. (2018). Slab2, a comprehensive subduction zone geometry model. *Science*, *362*(6410), 58–61. doi:10.1126/science.aat4723

Heimann, S., Isken, M., Kühn, D., Sudhaus, H., Steinberg, A., Vasyura-Bathke, H., … Dahm, T. (2018). *Grond - A probabilistic earthquake source inversion framework.* Retrieved from http://pyrocko.org/grond/docs/current/ doi:10.5880/GFZ.2.1.2018.003

Henrys, S., Reyners, M., Pecher, I., Bannister, S., Nishimura, Y., & Maslen, G. (2006). Kinking of the subducting slab by escalator normal faulting beneath the North Island of New Zealand. *Geology*, *34*(9), 777–780. doi:10.1130/G22594.1

Hicks, S. P., Okuwaki, R., Steinberg, A., Rychert, C. A., Harmon, N., Abercrombie, R. E., … Sudhaus, H. (2020). Back-propagating supershear rupture in the 2016 Mw 7.1 Romanche transform fault earthquake. *Nat. Geosci.*, *13*(9), 647–653. doi:10.1038/s41561-020-0619-9

Hicks, S. P., & Rietbrock, A. (2015). Seismic slip on an upper-plate normal fault during a large subduction megathrust rupture. *Nat. Geosci.*, *8*(12), 955–960. doi:10.1038/ngeo2585

Hong Kong Observatory. (2009). *Hong Kong Seismograph Network.* Retrieved from http://www.hko.gov.hk/gts/equake/sp_seismo_network_intro_e.htm

Hunter, J. D. (2007). Matplotlib: A 2D Graphics Environment. *Comput. Sci. Eng.*, *9*(3), 90–95. doi:10.1109/MCSE.2007.55

Institut De Physique Du Globe De Paris (IPGP), & Ecole Et Observatoire Des Sciences De La Terre De Strasbourg (EOST). (1982). *GEOSCOPE, French Global Network of broad band seismic stations.* Institut de physique du globe de Paris (IPGP), Université de Paris. doi:10.18715/GEOSCOPE.G

Institute of Geological & Nuclear Sciences Ltd (GNS New Zealand). (1988). *New Zealand National Seismograph Network.* Retrieved from https://www.fdsn.org/networks/detail/NZ/

International Seismological Centre. (2021). *On-line Bulletin.* doi:10.31905/D808B830

Istituto Nazionale Di Oceanografia E Di Geofisica Sperimentale. (1992). *Antarctic Seismographic Argentinean Italian Network - OGS.* International Federation of Digital Seismograph Networks. doi:10.7914/SN/AI

Kaneko, Y., Ito, Y., Chow, B., Wallace, L. M., Tape, C., Grapenthin, R., ... Hino, R. (2019). Ultra-long Duration of Seismic Ground Motion Arising From a Thick, Low-Velocity Sedimentary Wedge. *J. Geophys. Res. Solid Earth*, *124*(10), 10347–10359. doi:10.1029/2019JB017795

Kikuchi, M., & Kanamori, H. (1991). Inversion of complex body waves-III. *Bull. Seism. Soc. Am.*, *81*(6), 2335–2350. Retrieved from https://pubs.geoscienceworld.org/ssa/bssa/article-abstract/81/6/2335/102472/Inversion-of-complex-body-waves-III

Lay, T., Duputel, Z., Ye, L., & Kanamori, H. (2013). The December 7, 2012 Japan Trench intraplate doublet (Mw 7.2, 7.1) and interactions between near-trench intraplate thrust and normal faulting. *Phys. Earth Planet. Inter.*, *220*, 73–78. doi:10.1016/j.pepi.2013.04.009

Lay, T., Ye, L., Wu, Z., & Kanamori, H. (2020). Macrofracturing of Oceanic Lithosphere in Complex Large Earthquake Sequences. *J. Geophys. Res. Solid Earth*, *125*(10), 1–21. doi:10.1029/2020JB020137

Lewis, K. B., Collot, J. Y., & Lallemand, S. E. (1998). The dammed Hikurangi Trough: A channel-fed trench blocked by subducting seamounts and their wake avalanches (New Zealand-France GeodyNZ Project). *Basin Res.*, *10*(4), 441–468. doi:10.1046/j.1365-2117.1998.00080.x

Lewis, K. B., Lallemand, S. E., & Carter, L. (2004). Collapse in a quaternary shelf basin off East Cape, New Zealand: Evidence for passage of a subducted seamount inboard of the ruatoria giant avalanche. *New Zeal. J. Geol. Geophys.*, *47*(3), 415–429. doi:10.1080/00288306.2004.9515067

Lin, G., & Shearer, P. (2005). Tests of relative earthquake location techniques using synthetic data. *J. Geophys. Res. Solid Earth*, *110*(B4), 1–14. doi:10.1029/2004JB003380

Lin, G., & Shearer, P. (2006). The COMPLOC Earthquake Location Package. *Seismol. Res. Lett.*, *77*(4), 440–444. doi:10.1785/gssrl.77.4.440

Mason, W. G., Moresi, L., Betts, P. G., & Miller, M. S. (2010). Three-dimensional numerical models of the influence of a buoyant oceanic plateau on subduction zones. *Tectonophysics*, *483*(1-2), 71–79. doi:10.1016/j.tecto.2009.08.021

McGinty, P., Reyners, M., & Robinson, R. (2000). Stress directions in the shal-

low part of the Hikurangi subduction zone, New Zealand, from the inversion of earthquake first motions. *Geophys. J. Int.*, *142*(2), 339–350. doi:10.1046/j.1365-246X.2000.00155.x

Meng, L., Ampuero, J. P., Stock, J., Duputel, Z., Luo, Y., & Tsai, V. C. (2012). Earthquake in a maze: Compressional rupture branching during the 2012 Mw 8.6 Sumatra earthquake. *Science*, *337*(6095), 724–726. doi:10.1126/science.1224030

Mitchell, J. S., Mackay, K. A., Neil, H. L., Mackay, E. J., Pallentin, A., & Notman, P. (2012). Undersea New Zealand, 1: 5,000,000. *NIWA chart, Misc. Ser.*, *92*. Retrieved from https://niwa.co.nz/our-science/oceans/bathymetry/further-information

Miyazawa, M., & Mori, J. (2005). Detection of triggered deep low-frequency events from the 2003 Tokachi-oki earthquake. *Geophys. Res. Lett.*, *32*(10), 1–4. doi:10.1029/2005GL022539

Mochizuki, K., Henrys, S., Haijima, D., Warren-Smith, E., & Fry, B. (2021). Seismicity and velocity structure in the vicinity of repeating slow slip earthquakes, northern Hikurangi subduction zone, New Zealand. *Earth Planet. Sci. Lett.*, *563*, 116887. Retrieved from https://doi.org/10.1016/j.epsl.2021.116887 doi:10.1016/j.epsl.2021.116887

Nishikawa, T., & Ide, S. (2014). Earthquake size distribution in subduction zones linked to slab buoyancy. *Nat. Geosci.*, *7*(12), 904–908. doi:10.1038/ngeo2279

Ohta, Y., Miura, S., Ohzono, M., Kita, S., Linuma, T., Demachi, T., ... Umino, N. (2011). Large intraslab earthquake (2011 April 7, M 7.1) after the 2011 off the Pacific coast of Tohoku Earthquake (M 9.0): Coseismic fault model based on the dense GPS network data. *Earth, Planets Sp.*, *63*(12), 1207–1211. doi:10.5047/eps.2011.07.016

Okada, T., & Hasegawa, A. (2003). The M7.1 May 26, 2003 off-shore Miyagi Prefecture Earthquake in northeast Japan: Source process and aftershock distribution of an intra-slab event. *Earth, Planets Sp.*, *55*(12), 731–739. doi:10.1186/BF03352482

Okuwaki, R., Hirano, S., Yagi, Y., & Shimizu, K. (2020). Inchworm-like source evolution through a geometrically complex fault fueled persistent supershear rupture during the 2018 Palu Indonesia earthquake. *Earth Planet. Sci. Lett.*, *547*, 116449. doi:10.1016/j.epsl.2020.116449

Page, M. T., van Der Elst, N., Hardebeck, J., Felzer, K., & Michael, A. J. (2016). Three ingredients for improved global aftershock forecasts: Tectonic region, time-dependent catalog incompleteness, and intersequence variability. *Bull.*

687 *Seismol. Soc. Am.*, *106*(5), 2290–2301. doi:10.1785/0120160073
688 Petersen, T., Gledhill, K., Chadwick, M., Gale, N. H., & Ristau, J. (2011). The New
689 Zealand National Seismograph Network. *Seismol. Res. Lett.*, *82*(1), 9–20.
690 doi:10.1785/gssrl.82.1.9
691 Ranero, C. R., Villaseñor, A., Morgan, J. P., & Weinrebe, W. (2005). Relationship be-
692 tween bend-faulting at trenches and intermediate-depth seismicity. *Geochem-*
693 *istry, Geophys. Geosystems*, *6*(12). doi:10.1029/2005GC000997
694 Reyners, M., & McGinty, P. (1999). Shallow subduction tectonics in the Raukumara
695 Peninsula, New Zealand, as illuminated by earthquake focal mechanisms. *J.*
696 *Geophys. Res. Solid Earth*, *104*(B2), 3025–3034. doi:10.1029/1998JB900081
697 Richards-Dinger, K. B., & Shearer, P. M. (2000). Earthquake locations in southern
698 California obtained using source-specific station terms. *J. Geophys. Res. Solid*
699 *Earth*, *105*(B5), 10939–10960. doi:10.1029/2000JB900014
700 Romeo, I., & Álvarez-Gómez, J. A. (2018). Lithospheric folding by flexural slip in
701 subduction zones as source for reverse fault intraslab earthquakes. *Sci. Rep.*,
702 *8*(1), 1–9. doi:10.1038/s41598-018-19682-7
703 Sandiford, D., Moresi, L., Sandiford, M., & Yang, T. (2019). Geometric
704 controls on flat slab seismicity. *Earth Planet. Sci. Lett.*, *527*, 115787.
705 doi:10.1016/j.epsl.2019.115787
706 Sandiford, D., Moresi, L. M., Sandiford, M., Farrington, R., & Yang, T. (2020).
707 The Fingerprints of Flexure in Slab Seismicity. *Tectonics*, *39*(8).
708 doi:10.1029/2019TC005894
709 Scripps Institution Of Oceanography. (1986). *IRIS/IDA Seismic Network.* Interna-
710 tional Federation of Digital Seismograph Networks. doi:10.7914/SN/II
711 Shimizu, K., Yagi, Y., Okuwaki, R., & Fukahata, Y. (2020). Development of an inver-
712 sion method to extract information on fault geometry from teleseismic data.
713 *Geophys. J. Int.*, *220*(2), 1055–1065. doi:10.1093/gji/ggz496
714 Shimizu, K., Yagi, Y., Okuwaki, R., & Fukahata, Y. (2021). Construction of fault
715 geometry by finite-fault inversion of teleseismic data. *Geophys. J. Int.*, *224*(2),
716 1003–1014. doi:10.1093/gji/ggaa501
717 Simons, M., Fialko, Y., & Rivera, L. (2002). Coseismic deformation from the
718 1999 Mw 7.1 Hector Mine, California, earthquake as inferred from In-
719 SAR and GPS observations. *Bull. Seismol. Soc. Am.*, *92*(4), 1390–1402.
720 doi:10.1785/0120000933
721 Sippl, C., Schurr, B., Asch, G., & Kummerow, J. (2018). Seismicity Struc-
722 ture of the Northern Chile Forearc From >100,000 Double-Difference
723 Relocated Hypocenters. *J. Geophys. Res. Solid Earth*, *123*(5), 4063–4087.

724 doi:10.1002/2017JB015384

725 Sleep, N. H., & Ma, S. (2008). Production of brief extreme ground acceleration
726 pulses by nonlinear mechanisms in the shallow subsurface. *Geochemistry, Geo-*
727 *phys. Geosystems*, *9*(3), Q03008. doi:10.1029/2007GC001863

728 Tadapansawut, T., Okuwaki, R., Yagi, Y., & Yamashita, S. (2021). Rupture Process of
729 the 2020 Caribbean Earthquake Along the Oriente Transform Fault, Involving
730 Supershear Rupture and Geometric Complexity of Fault. *Geophys. Res. Lett.*,
731 *48*(1), 1–9. doi:10.1029/2020GL090899

732 Tanioka, Y., Ruff, L., & Satake, K. (1995). The great Kurile Earthquake of
733 October 4, 1994 tore the slab. *Geophys. Res. Lett.*, *22*(13), 1661–1664.
734 doi:10.1029/95GL01656

735 The Pyrocko Developers. (2017). *Pyrocko: A Versatile Seismology Toolkit for Python.*
736 Retrieved from http://pyrocko.org doi:10.5880/GFZ.2.1.2017.001

737 Todd, E. K., & Lay, T. (2013). The 2011 Northern Kermadec earthquake doublet and
738 subduction zone faulting interactions. *J. Geophys. Res. Solid Earth*, *118*(1), 249–
739 261. doi:10.1029/2012JB009711

740 Universidad de Chile Dept de Geofisica (DGF UChile Chile). (1991). *Chilean Na-*
741 *tional Seismic Network.* Retrieved from https://www.fdsn.org/networks/
742 detail/C/

743 University of Tokyo Earthquake Research Institute (Todai ERI Japan). (1989). *Pa-*
744 *cific21 (ERI/STA).* Retrieved from https://www.fdsn.org/networks/detail/
745 PS/

746 U.S. Geological Survey Earthquake Hazards Program. (2017). *Advanced National*
747 *Seismic System (ANSS) Comprehensive Catalog of Earthquake Events and Prod-*
748 *ucts.* doi:10.5066/F7MS3QZH

749 Wallace, L. M., Reyners, M., Cochran, U., Bannister, S., Barnes, P. M., Berryman, K.,
750 ... Power, W. (2009). Characterizing the seismogenic zone of a major plate
751 boundary subduction thrust: Hikurangi Margin, New Zealand. *Geochemistry,*
752 *Geophys. Geosystems*, *10*(10). doi:10.1029/2009GC002610

753 Wang, K., & Bilek, S. L. (2011). Do subducting seamounts generate or stop large
754 earthquakes? *Geology*, *39*(9), 819–822. doi:10.1130/G31856.1

755 Wessel, P., & Luis, J. F. (2017). The GMT/MATLAB Toolbox. *Geochemistry, Geophys.*
756 *Geosystems*, *18*(2), 811–823. doi:10.1002/2016GC006723

757 Wiens, D. A. (2001). Seismological constraints on the mechanism of deep earth-
758 quakes: Temperature dependence of deep earthquake source properties. *Phys.*
759 *Earth Planet. Inter.*, *127*(1-4), 145–163. doi:10.1016/S0031-9201(01)00225-4

760 Williams, C. A., Eberhart-Phillips, D., Bannister, S., Barker, D. H., Henrys, S., Reyn-

761 ers, M., & Sutherland, R. (2013). Revised interface geometry for the hiku-
762 rangi subduction zone, New Zealand. *Seismol. Res. Lett.*, *84*(6), 1066–1073.
763 doi:10.1785/0220130035
764 Wiseman, K., Banerjee, P., Bürgmann, R., Sieh, K., Dreger, D. S., & Hermawan,
765 I. (2012). Source model of the 2009 Mw 7.6 Padang intraslab earthquake
766 and its effect on the Sunda megathrust. *Geophys. J. Int.*, *190*(3), 1710–1722.
767 doi:10.1111/j.1365-246X.2012.05600.x
768 Yabuki, T., & Matsu'ura, M. (1992). Geodetic data inversion using a Bayesian
769 information criterion for spatial distribution of fault slip. *Geophys. J. Int.*,
770 *109*(2), 363–375. Retrieved from https://onlinelibrary.wiley.com/doi/
771 abs/10.1111/j.1365-246X.1992.tb00102.xhttps://academic.oup.com/gji/
772 article-lookup/doi/10.1111/j.1365-246X.1992.tb00102.x doi:10.1111/j.1365-
773 246X.1992.tb00102.x
774 Yamashita, S., Yagi, Y., Okuwaki, R., Shimizu, K., Agata, R., & Fukahata, Y. (2021).
775 Consecutive ruptures on a complex conjugate fault system during the 2018
776 Gulf of Alaska earthquake. *Sci. Rep.*, *11*(1), 5979. doi:10.1038/s41598-021-
777 85522-w
778 Ye, L., Lay, T., Bai, Y., Cheung, K. F., & Kanamori, H. (2017). The 2017 Mw 8.2
779 Chiapas, Mexico, Earthquake: Energetic Slab Detachment. *Geophys. Res. Lett.*,
780 *44*(23), 11,824–11,832. doi:10.1002/2017GL076085
781 Ye, L., Lay, T., & Kanamori, H. (2012). Intraplate and interplate faulting interactions
782 during the August 31, 2012, Philippine Trench earthquake (Mw 7.6) sequence.
783 *Geophys. Res. Lett.*, *39*(24), 1–6. doi:10.1029/2012GL054164
784 Ye, L., Lay, T., & Kanamori, H. (2021). The 25 March 2020 Mw 7.5 Paramushir,
785 northern Kuril Islands earthquake and major (Mw≥7.0) near-trench intraplate
786 compressional faulting. *Earth Planet. Sci. Lett.*, *556*(March 2020), 116728.
787 doi:10.1016/j.epsl.2020.116728
788 Yue, H., Lay, T., & Koper, K. D. (2012). En échelon and orthogonal fault ruptures
789 of the 11 April 2012 great intraplate earthquakes. *Nature*, *490*(7419), 245–249.
790 doi:10.1038/nature11492

791 References From the Supporting Information

792 Ampuero, J.-P., & Dahlen, F. A. (2005). Ambiguity of the Moment Tensor. *Bull. Seis-*
793 *mol. Soc. Am.*, *95*(2), 390–400. doi:10.1785/0120040103
794 Bassett, D., Sutherland, R., Henrys, S., Stern, T., Scherwath, M., Benson, A., ... Hen-
795 derson, M. (2010). Three-dimensional velocity structure of the northern
796 Hikurangi margin, Raukumara, New Zealand: Implications for the growth of

continental crust by subduction erosion and tectonic underplating. *Geochemistry, Geophys. Geosystems*, *11*(10). doi:10.1029/2010GC003137

Bird, P. (2003). An updated digital model of plate boundaries. *Geochemistry, Geophys. Geosystems*, *4*(3), 1105. doi:10.1029/2001GC000252

Bormann, P. (2012). New Manual of Seismological Observatory Practice (NMSOP-2). *IASPEI, GFZ Ger. Res. Cent. Geosci.*. doi:10.2312/GFZ.NMSOP-2

Duputel, Z., Rivera, L., Kanamori, H., & Hayes, G. (2012). W phase source inversion for moderate to large earthquakes (1990-2010). *Geophys. J. Int.*, *189*(2), 1125–1147. doi:10.1111/j.1365-246X.2012.05419.x

Dziewonski, A. M., Chou, T.-A., & Woodhouse, J. H. (1981). Determination of earthquake source parameters from waveform data for studies of global and regional seismicity. *J. Geophys. Res. Solid Earth*, *86*(B4), 2825–2852. doi:10.1029/JB086iB04p02825

Eberhart-Phillips, D., Bannister, S., Reyners, M., & Henrys, S. (2020). *New Zealand Wide model 2.2 seismic velocity and Qs and Qp models for New Zealand.* Zenodo. doi:10.5281/zenodo.3779523

Eberhart-Phillips, D., Reyners, M., Bannister, S., Chadwick, M., & Ellis, S. (2010). Establishing a versatile 3-D seismic velocity model for New Zealand. *Seismol. Res. Lett.*, *81*(6), 992–1000. doi:10.1785/gssrl.81.6.992

Ekström, G., Nettles, M., & Dziewoński, A. (2012). The global CMT project 2004–2010: Centroid-moment tensors for 13,017 earthquakes. *Phys. Earth Planet. Inter.*, *200-201*, 1–9. doi:10.1016/j.pepi.2012.04.002

GeoNet. (2021). *GeoNet Earthquake Catalog.* Retrieved from https://www.geonet.org.nz/data/types/eq_catalogue

GeoNet Moment Tensors. (2021). *GeoNet Moment Tensors.* Retrieved from https://github.com/GeoNet/data/tree/main/moment-tensor

Hayes, G. P. (2018). *Slab2 - A Comprehensive Subduction Zone Geometry Model: U.S. Geological Survey data release.* doi:10.5066/F7PV6JNV

Hayes, G. P., Moore, G. L., Portner, D. E., Hearne, M., Flamme, H., Furtney, M., & Smoczyk, G. M. (2018). Slab2, a comprehensive subduction zone geometry model. *Science*, *362*(6410), 58–61. doi:10.1126/science.aat4723

Heimann, S., Isken, M., Kühn, D., Sudhaus, H., Steinberg, A., Vasyura-Bathke, H., ... Dahm, T. (2018). *Grond - A probabilistic earthquake source inversion framework.* Retrieved from http://pyrocko.org/grond/docs/current/ doi:10.5880/GFZ.2.1.2018.003

Kennett, B. L., Engdahl, E. R., & Buland, R. (1995). Constraints on seismic velocities in the Earth from traveltimes. *Geophys. J. Int.*, *122*(1), 108–124.

834 doi:10.1111/j.1365-246X.1995.tb03540.x
835 Kikuchi, M., & Kanamori, H. (1991). Inversion of complex body waves-
836 III. *Bull. Seism. Soc. Am.*, *81*(6), 2335–2350. Retrieved from https://
837 pubs.geoscienceworld.org/ssa/bssa/article-abstract/81/6/2335/102472/
838 Inversion-of-complex-body-waves-III
839 Laske, G., Masters, T. G., Ma, Z., & Pasyanos, M. (2013). Update on CRUST1.0
840 - A 1-degree Global Model of Earth's Crust. *Geophys. Res. Abstr. 15*, *Ab-*
841 *str. EGU2013-2658*, *15*, Abstract EGU2013–2658. Retrieved from https://
842 igppweb.ucsd.edu/~gabi/crust1.html
843 Lin, G., & Shearer, P. (2005). Tests of relative earthquake location tech-
844 niques using synthetic data. *J. Geophys. Res. Solid Earth*, *110*(B4), 1–14.
845 doi:10.1029/2004JB003380
846 Lin, G., & Shearer, P. (2006). The COMPLOC Earthquake Location Package. *Seismol.*
847 *Res. Lett.*, *77*(4), 440–444. doi:10.1785/gssrl.77.4.440
848 Lomax, A., Michelini, A., & Curtis, A. (2009). Earthquake Location, Direct, Global-
849 Search Methods BT - Encyclopedia of Complexity and Systems Science. *Encycl.*
850 *Complex. Syst. Sci.*, 2449–2473. doi:10.1007/978-0-387-30440-3_150
851 Lomax, A., Virieux, J., Volant, P., & Berge-Thierry, C. (2000). Probabilistic Earth-
852 quake Location in 3D and Layered Models BT - Advances in Seismic Event
853 Location. In C. H. Thurber & N. Rabinowitz (Eds.), (pp. 101–134). Dordrecht:
854 Springer Netherlands. doi:10.1007/978-94-015-9536-0_5
855 Okuwaki, R., Hirano, S., Yagi, Y., & Shimizu, K. (2020). Inchworm-like source
856 evolution through a geometrically complex fault fueled persistent supershear
857 rupture during the 2018 Palu Indonesia earthquake. *Earth Planet. Sci. Lett.*,
858 *547*, 116449. doi:10.1016/j.epsl.2020.116449
859 Okuwaki, R., Yagi, Y., Aránguiz, R., González, J., & González, G. (2016). Rupture
860 Process During the 2015 Illapel, Chile Earthquake: Zigzag-Along-Dip Rupture
861 Episodes. *Pure Appl. Geophys.*, *173*(4), 1011–1020. doi:10.1007/s00024-016-
862 1271-6
863 Petersen, T., Gledhill, K., Chadwick, M., Gale, N. H., & Ristau, J. (2011). The New
864 Zealand National Seismograph Network. *Seismol. Res. Lett.*, *82*(1), 9–20.
865 doi:10.1785/gssrl.82.1.9
866 Shimizu, K., Yagi, Y., Okuwaki, R., & Fukahata, Y. (2020). Development of an inver-
867 sion method to extract information on fault geometry from teleseismic data.
868 *Geophys. J. Int.*, *220*(2), 1055–1065. doi:10.1093/gji/ggz496
869 Shimizu, K., Yagi, Y., Okuwaki, R., & Fukahata, Y. (2021). Construction of fault
870 geometry by finite-fault inversion of teleseismic data. *Geophys. J. Int.*, *224*(2),

1003–1014. doi:10.1093/gji/ggaa501

Sokos, E. N., & Zahradnik, J. (2008). ISOLA a Fortran code and a Matlab GUI to perform multiple-point source inversion of seismic data. *Comput. Geosci.*, *34*(8), 967–977. doi:10.1016/j.cageo.2007.07.005

Tadapansawut, T., Okuwaki, R., Yagi, Y., & Yamashita, S. (2021). Rupture Process of the 2020 Caribbean Earthquake Along the Oriente Transform Fault, Involving Supershear Rupture and Geometric Complexity of Fault. *Geophys. Res. Lett.*, *48*(1), 1–9. doi:10.1029/2020GL090899

U.S. Geological Survey Earthquake Hazards Program. (2017). *Advanced National Seismic System (ANSS) Comprehensive Catalog of Earthquake Events and Products.* doi:10.5066/F7MS3QZH

Vallée, M. (2013). Source time function properties indicate a strain drop independent of earthquake depth and magnitude. *Nat. Commun.*, *4*, 1–6. doi:10.1038/ncomms3606

Vallée, M., Charléty, J., Ferreira, A. M., Delouis, B., & Vergoz, J. (2011). SCARDEC: A new technique for the rapid determination of seismic moment magnitude, focal mechanism and source time functions for large earthquakes using body-wave deconvolution. *Geophys. J. Int.*, *184*(1), 338–358. doi:10.1111/j.1365-246X.2010.04836.x

Yagi, Y., & Fukahata, Y. (2011). Introduction of uncertainty of Green's function into waveform inversion for seismic source processes. *Geophys. J. Int.*, *186*(2), 711–720. doi:10.1111/j.1365-246X.2011.05043.x

Yamashita, S., Yagi, Y., Okuwaki, R., Shimizu, K., Agata, R., & Fukahata, Y. (2021). Consecutive ruptures on a complex conjugate fault system during the 2018 Gulf of Alaska earthquake. *Sci. Rep.*, *11*(1), 5979. doi:10.1038/s41598-021-85522-w

Ye, L., Lay, T., Bai, Y., Cheung, K. F., & Kanamori, H. (2017). The 2017 Mw 8.2 Chiapas, Mexico, Earthquake: Energetic Slab Detachment. *Geophys. Res. Lett.*, *44*(23), 11,824–11,832. doi:10.1002/2017GL076085